Toroidal flow measurements of impurity ions in QUEST ECH plasmas using multiple viewing chords emission spectroscopy

AUTHOR(S):

Yoneda, N.; Shikama, T.; Hanada, K.; Mori, S.; Onchi, T.; Kuroda, K.; Hasuo, M.; ... Higashijima, A.; Nagata, T.; Shimabukuro, S.

CITATION:

Yoneda, N. ...[et al]. Toroidal flow measurements of impurity ions in QUEST ECH plasmas using multiple viewing chords emission spectroscopy. Nuclear Materials and Energy 2021, 26: 100905.

ISSUE DATE:

2021-03

URL:

http://hdl.handle.net/2433/277795

Nuclear Materials and Energy 26 (2021) 100905

Contents lists available at ScienceDirect

Nuclear Materials and Energy

journal homepage: www.elsevier.com/locate/nme

Toroidal flow measurements of impurity ions in QUEST ECH plasmas using multiple viewing chords emission spectroscopy

N. Yoneda [a,*], T. Shikama [a], K. Hanada [b], S. Mori [a], T. Onchi [b], K. Kuroda [b], M. Hasuo [a], A. Ejiri [c], K. Matsuzaki [c], Y. Osawa [c], Y. Peng [c], Y. Kawamata [c], S. Sakamoto [c], H. Idei [b], T. Ido [b], K. Nakamura [b], Y. Nagashima [b], R. Ikezoe [b], M. Hasegawa [b], A. Higashijima [b], T. Nagata [b], S. Shimabukuro [b]

[a] Department of Mechanical Engineering and Science, Kyoto University, Kyoto 615-8540, Japan
[b] Research Institute for Applied Mechanics, Kyushu University, Fukuoka 816-8580, Japan
[c] Graduate School of Frontier Science, The University of Tokyo, Kashiwa 277-8561, Japan

ARTICLE INFO

Keywords:
Spherical tokamak
ECH
Magnetic configuration
Toroidal flow
Emission spectroscopy
Inversion

ABSTRACT

A spectroscopic system with multiple viewing chords was developed for QUEST (Q-shu University Experiment with Steady-State Spherical Tokamak) to measure the spatial distribution of ion toroidal velocities in discharges sustained by electron cyclotron resonance heating (ECH). Twenty-four viewing chords were aligned in the midplane and C III emission line spectra were measured for three types of ECH discharge under different magnetic field configurations. By applying an inversion method to the measured spectra, we evaluated the radial distributions of C^{2+} ion emissivity, temperature, and toroidal velocity. The error in the evaluated velocity was estimated to be less than 5 km/s. It was found that the velocity depends on the magnetic field configuration.

1. Introduction

The development of a noninductive discharge startup method is important for spherical tokamaks to reduce the sizes of central solenoid coils. A candidate method is a startup with electron cyclotron resonance heating (ECH) [1,2] and its capability has been studied in QUEST (Q-shu University Experiment with Steady-State Spherical Tokamak) using two types of microwave source (8.2 and 28 GHz) under two different magnetic field configurations (inboard limiter and inboard poloidal null).

In these ECH discharges, variation in C^{2+} ion toroidal velocity with the magnetic field configuration was suggested in a previous research [3]. The profile of the toroidal velocity could be controlled by changing the magnetic field configuration. To further investigate the spatial distribution of the velocity and its dependence on the magnetic field configuration, we have developed a spectroscopy system with high wavelength resolution and multiple viewing chords in the midplane. Emission spectroscopy was used for the measurement instead of charge exchange recombination spectroscopy because ECH discharges have no neutral beam injection. We measured C III emission line spectra in three types of discharge and evaluated radially resolved ion emissivity, temperature, and toroidal velocity by an inversion method.

2. Experimental setup

2.1. Discharges

QUEST is a medium-sized spherical tokamak, which has the major and minor radii of 0.64 and 0.46 m, respectively. As illustrated in Figs. 1 and 3, the first walls consist of an inboard limiter and a radiation shield located at $R = 0.22$ and 1.30 m, respectively, and the top and bottom divertor plates located at $z = 1.0$ and -1.1 m.

During the startup by ECH, a cylindrical plasma with open magnetic flux surfaces is initially produced around the resonance layer, and then a closed flux surface is formed by rapidly increasing plasma current. In QUEST, three types of discharge have been established to date: (i) the inboard limiter (IL) configuration with 8.2 GHz ECH (8.2 GHz IL), (ii) the IL configuration with 28 GHz ECH (28 GHz IL) [4] and (iii) the inboard poloidal null (IPN) configuration with 8.2 GHz ECH (8.2 GHz IPN) [5].

For cylindrical plasmas in QUEST, emissivity-weighted toroidal velocities of C^{2+} ions were measured. Their directions were the same as those of the Pfirsch–Schlüter flow, and their velocities increased with the strength of the superposed vertical field [6]. For the transitional

* Corresponding author.
E-mail address: yoneda.nao.45m@st.kyoto-u.ac.jp (N. Yoneda).

https://doi.org/10.1016/j.nme.2021.100905
Received 31 July 2020; Received in revised form 23 December 2020; Accepted 5 January 2021
Available online 13 January 2021

phase from the cylindrical plasmas to discharges with closed flux surfaces, the scale of the temporal evolution was shorter than the minimum exposure time required to obtain analyzable data. Thus, we focused on the flat-top phase of the three types of discharge with closed flux surfaces when the ECH power, the currents of the magnetic coils, and the plasma current were constant.

Table 1 shows plasma parameters during the flat-top phase. Under the IL configurations, the last closed flux surface (LCFS) is tangent to the inboard limiter (Figs. 1(i) and (ii)), and under the IPN configuration, it has a poloidal null at the inboard midplane (Fig. 1(iii)). In 8.2 GHz ECH discharges (i) and (iii), the fundamental and second-harmonic resonance layers exist in the plasma at $R_{res} = 0.29$ m ($B = 0.29$ T) and 0.57 m (0.15 T), respectively, whereas in 28 GHz ECH discharge (iii), the second-harmonic layer exists at $R = 0.32$ m ($B = 0.50$ T). The radial distributions of the electron density n_e and temperature T_e in the midplane measured by Thomson scattering in the flat-top phase are shown in Fig. 2 [7].

2.2. Spectroscopic system

We evaluated the toroidal flow velocity of C^{2+} ions from the Doppler shift of the C III (464.742 nm) emission line. Fig. 3 shows the spectroscopic system, which consists of four optical-fiber bundles, a spectrometer, and a CCD camera [8]. We denote the fiber bundles as bundles A, B, C and D. The former two and the latter two respectively contain 27 and 15 fibers (Mitsubishi Cable Industries, STU230D; 230 and 250 μm core and clad diameters, respectively, and 0.2 NA). Bundles C and D combined with lenses (Edmund Optics, TS achromatic lens 15x15 MGF2; 15 mm focal length and 14 mm diameter) were used to collect plasma emission, and bundle B was used to collect He–Ne discharge tube emission (NEC, GLG5000) as a wavelength reference. Twenty-seven optical fibers from these three bundles, 3, 11, and 13 fibers of B, C, and D, respectively, were connected to a Czerny–Turner spectrometer (Acton Research, AM-510; 1 m focal length, F/8.7, and 1800 grooves/mm grating) via bundle A. The collected emission enters into the spectrometer through a slit of 50 μm width and an astigmatism compensation system, which consists of two concave mirrors (Tokyo Instruments; 0.3 m focal length). The dispersed spectra were recoded using a CCD camera (Andor Technology, DU440-BU2; 2048 × 512 pixels and 13.5 μm square pixels). The central wavelength of the spectrometer was set to 468 nm. The reciprocal linear dispersion was 6.4 pm/pixel and the simultaneously measured wavelengths were in the range of 461.2–474.2 nm.

Table 1
Parameters of (i) 8.2 GHz IL, (ii) 28 GHz IL, and (iii) 8.2 GHz IPN discharges. t_{plasma} is the plasma duration, and the time of the flat-top phase is shown in parentheses. The following plasma parameters are for the flat-top phase. P_{ECH} is the ECH power, B_φ is the toroidal field strength at the magnetic axis, and I_p is the plasma current. R_{res}, R_{axis}, and R_{LCFS} are the radial positions of the resonance layer, magnetic axis, and LCFS, respectively. n_e and T_e are the electron density and temperature measured by Thomson scattering [7]. η is the tangency radius of each viewing chord, and its range is shown in the column. t_{exp} is the exposure time of the CCD.

	(i) 8.2 GHz IL	(ii) 28 GHz IL	(iii) 8.2 GHz IPN
t_{plasma} [s]	15 (15)	1.3 (0.2)	15 (15)
P_{ECH} [kW]	50	120	50
B_φ@axis [T]	0.1	0.5	0.1
I_p [kA]	4	25.4	7
R_{res} [m]	0.29 (1st), 0.57 (2nd)	0.32 (2nd)	0.29 (1st), 0.57 (2nd)
R_{axis} [m]	0.7	0.3	0.6
R_{LCFS} [m]	1.1	0.4	0.7
n_e@axis [m^{-3}]	1×10^{17}	1×10^{18}	5×10^{16}
T_e@axis [eV]	40	300	100
η [m]	0.31–0.95	0.24–1.01	0.31–0.95
t_{exp} [s]	1	0.13	1

Twenty-four viewing chords were aligned in the midplane using bundles C and D. Fig. 3 shows the viewing chords used for measurements in discharges (i) and (iii). η is the tangency radius of each viewing chord. As shown in Table 1, η ranges from 0.31 to 0.95 m for discharges (i) and (iii). The wider radial view, $\eta = 0.24$–1.01 m, was used for discharge (ii), which is the same setup as that used in [8] (see Fig. 2 of Ref. 8). The diameter of each viewing chord was approximately 30 mm. For three pairs of adjacent viewing chords of the setup used for discharges (i) and (iii), the differences in η between the adjacent viewing chords were about 8 mm and smaller than the diameter. We averaged the spectra measured on the adjacent viewing chords, which reduced the number of viewing chords used for analysis to 21 for discharges (i) and (iii).

The wavelengths of observed spectra were absolutely calibrated using Ne I emission lines of known wavelengths [12] and their intensity

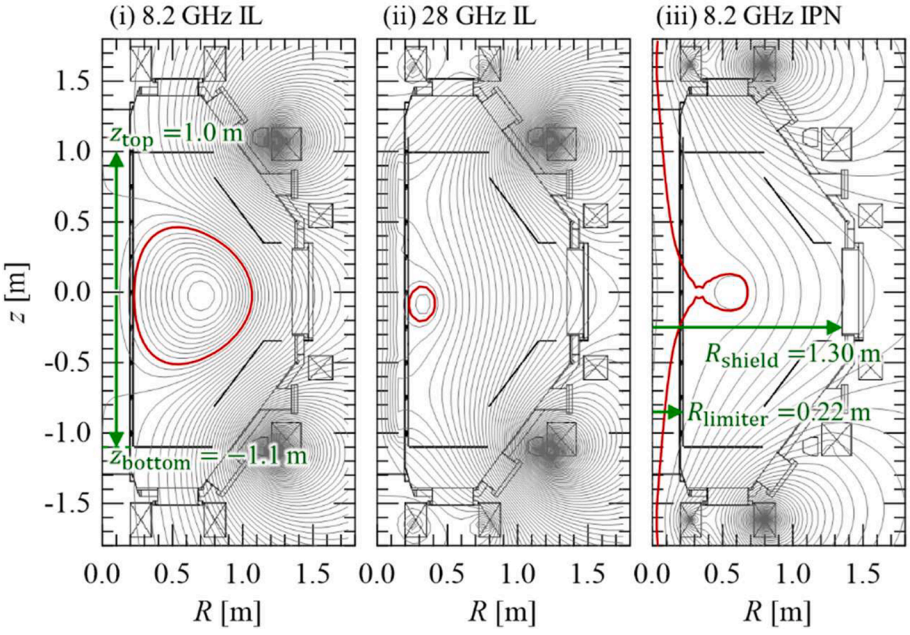

Fig. 1. Poloidal cross sections of QUEST with flux surfaces at (i) 8.2 GHz IL, (ii) 28 GHz IL, and (iii) 8.2 GHz IPN discharges. Red lines show the last flux surfaces. Height positions of the top and bottom divertor plates are shown as z_{top} and z_{bottom}, respectively, in (i). Radial positions of the inboard limiter and radiation shield are shown as $R_{limiter}$ and R_{shield}, respectively, in (iii). (For interpretation of the references to colour in this figure legend, the reader is referred to the web version of this article.)

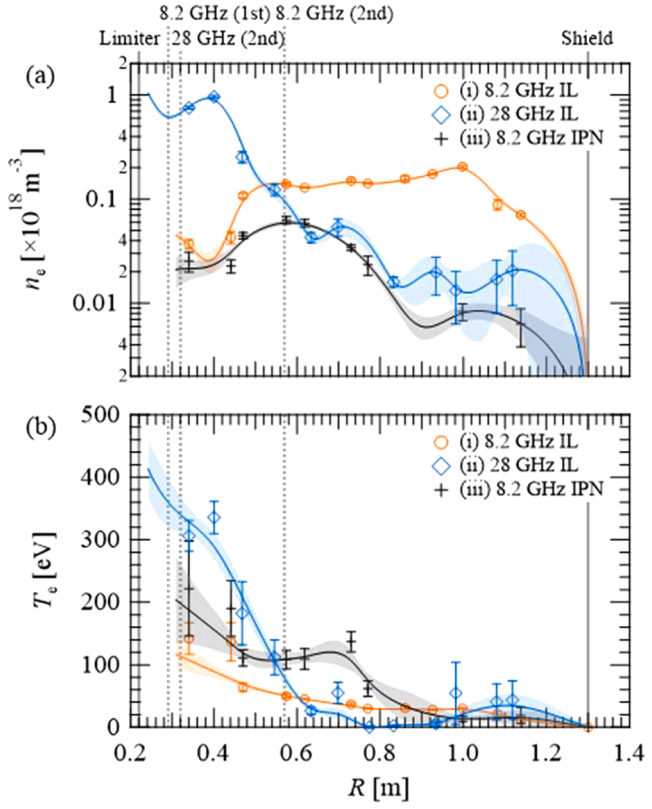

Fig. 2. (a) Electron density, (b) electron temperature measured by Thomson scattering. Markers and curves are measured data and the interpolation and extrapolation by smoothing spline [14], respectively. Solid vertical lines show the positions of the inboard limiter (Limiter) and radiation shield (Shield), respectively. Dotted vertical lines show the positions of the resonance layers for 8.2 GHz ECH (8.2 GHz (1st) and 8.2 GHz (2nd)) and 28 GHz ECH (28 GHz (2nd)).

was also absolutely calibrated using continuum spectra from a standard tungsten-halogen lamp (Ushio Lighting, 212012) or a xenon standard lamp (Hamamatsu Photonics, L7810-02). To reduce systematic errors in the calibrated wavelength produced by room temperature variation, we measured the Ne I emission lines immediately after the discharges [6]. This procedure reduced the errors to less than 0.4 pm, which correspond to a toroidal velocity of less than 0.3 km/s.

The instrumental function was measured using a Ne I emission line spectrum at 464.9904 nm, whose Doppler broadening is negligible. Owing to slight misalignment of the astigmatism compensation system, the instrumental function has a wider and asymmetric shape at the upper part of the CCD, which corresponds to viewing chords at smaller η. We used a double Gaussian function with the same standard deviation to approximate the instrumental function. The instrumental width was estimated to be 20.2–43.9 pm at FWHM depending on the viewing chords.

We measured spectra in the flat-top phase of the discharges with the CCD exposure time of 1 s for discharges (i) and (iii) and 0.13 s for discharge (ii) (see Table 1). Fig. 4 shows a spectrum measured on a viewing chord at $\eta = 0.78$ m in discharge (iii). The red and green bars respectively show the wavelengths of C III and O II emission lines cited from the NIST database [12]. We have roughly calculated the velocity relaxation time of the C^{2+} and O^{+} impurity ions with bulk H^{+} ion collisions [9,10]. The following parameters were used for the calculations: H^{+} ion density $n_{H^+} = 10^{17}$ [m^{-3}], impurity ion density $n_{imp} = 10^{16}$ [m^{-3}], and H^{+} and impurity ion temperature $T_{H^+} = T_{imp} = 10$ [eV]. The parameters were determined from the results of Thomson scattering [7] (assuming $n_e \approx n_{H^+}$) and spectroscopic measurements. The derived relaxation times were 0.4 and 2 ms for C^{2+} and O^{+} ions, respectively. Because of the shorter relaxation time, we focused on the emission from

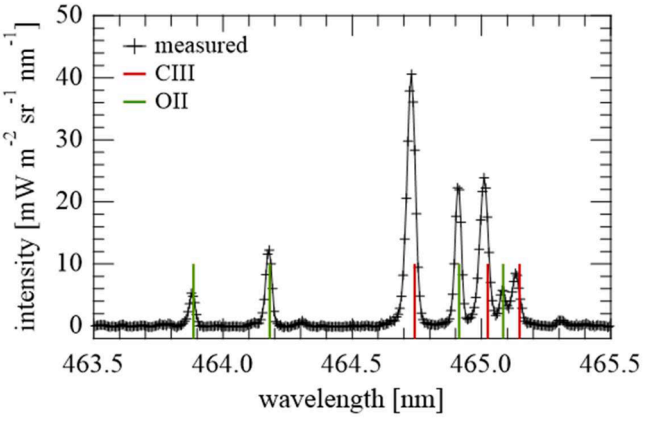

Fig. 4. Example of spectrum measured for (iii) 8.2 GHz IPN discharge ($\eta = 0.78$ m).

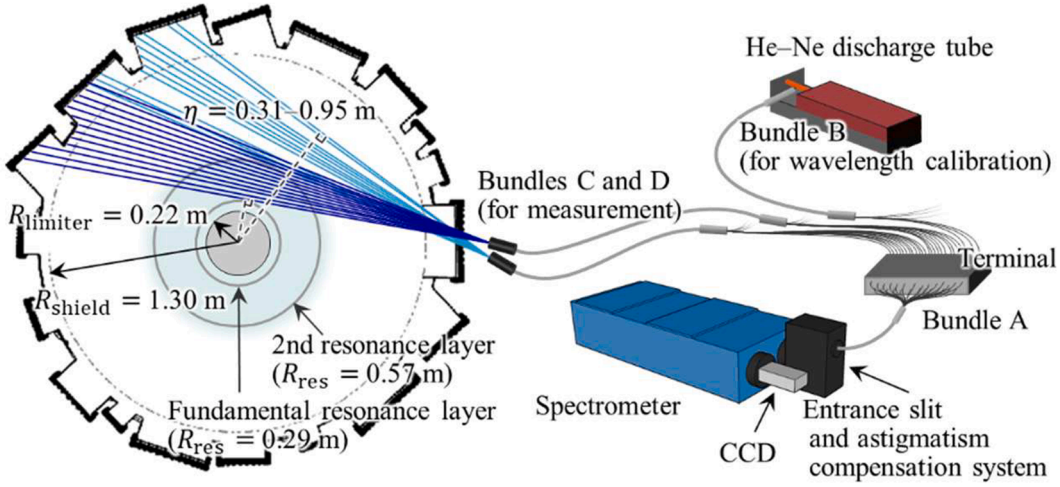

Fig. 3. Schematics of the spectroscopic system. Viewing chords used for the measurements of (i) 8.2 GHz IL and (iii) 8.2 GHz IPN discharges are shown with the midplane of QUEST. Light blue and blue lines correspond to viewing chords of bundles C and D, respectively. η is the tangency radius of each viewing chord. (For interpretation of the references to colour in this figure legend, the reader is referred to the web version of this article.)

C^{2+} ions. We analyzed the C III emission line at 464.742 nm ($1s^2 2s3s\ ^3S_1 - 1s^2 2s3p\ ^3P^o_2$), and the line spectrum was isolated and had a sufficiently large signal-to-noise ratio.

3. Analysis

3.1. Inversion method

The markers in Figs. 6(a) and (b) show the intensity I_A calculated from the area of the chord-integrated spectra and the emissivity-weighted velocity V evaluated by a single Gaussian fitting to the spectra. We applied an inversion method assuming an axisymmetry of the plasmas to estimate the radially resolved toroidal velocity V_φ. Firstly, we evaluated the radially resolved emissivity ε from I_A using the Abel inversion, and then evaluated V_φ and the radially resolved ion temperature T_i by an inversion method using the "shell model" [11].

In the first step, we evaluated the continuous radial distribution of the emissivity $\varepsilon(R)$ as

$$\varepsilon(R) = -\frac{1}{\pi}\int_R^{R_{end}} \frac{1}{\sqrt{\eta^2 - R^2}} \frac{dI_A(\eta)}{d\eta} d\eta, \tag{1}$$

where R_{end} is the outer boundary of the emission. We interpolated the measured I_A with a single or double sigmoid function, as shown in Fig. 6 (a) with the solid lines, and determined R_{end} to be a position where the extrapolated curve becomes zero. The error of ε was estimated by the following six steps: (I) calculate the 68.3% confidence interval when I_A is interpolated, (II) estimate the standard deviation of I_A by regarding the confidence interval as the standard deviation, (III) generate 500 datasets by adding Gaussian noise with the estimated standard deviation to the measured I_A, (IV) interpolate the datasets, (V) apply the Abel inversion to the dataset, and (VI) calculate the mean and standard deviation of the derived ε for each radial position R. The mean and standard deviation were plotted as the value and standard deviation of ε in Fig. 6(c).

In the second step, we divided the midplane into concentric regions called "shells", as shown in Fig. 5, and assumed that V_φ and T_i are uniform in each shell. We denote the viewing chords as chords 1, 2, 3, … and the shells as shells 1, 2, 3, … from the outboard side (see Fig. 5). The radii of shell boundaries were determined such that they became means of η of the adjacent two viewing chords. The radius of the outermost shell boundary was set to R_{end}.

Since chord k intersects with shells 1, 2, …, and k, a spectrum chord-integrated along chord k ($I_k(\lambda)$) is expressed by the sum of spectra from intersecting shells as

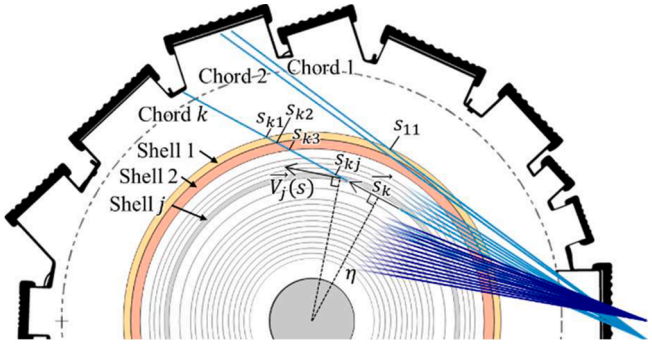

Fig. 5. Schematics of the second inversion method: shell model. Light blue and blue lines show the viewing chords used for the measurements of 8.2 GHz ECH discharges. Gray concentric circles show the boundaries of shells, and shells 1, 2, and j are colored yellow, orange, and gray, respectively. (For interpretation of the references to colour in this figure legend, the reader is referred to the web version of this article.)

$$I_k(\lambda) = \sum_{j=1}^{k} I_{kj}(\lambda), \tag{2}$$

where $I_{kj}(\lambda)$ is the emission line spectrum from shell j. $I_{kj}(\lambda)$ is expressed as a function of the toroidal velocity $V_{\varphi,j}$ and temperature $T_{i,j}$ in shell j as

$$I_{kj}(\lambda) = 2\gamma_k \int_{s_{k(j+1)}}^{s_{kj}} \frac{\varepsilon(s_k)}{\sqrt{2\pi}w_j} \exp\left\{ -\frac{\left[\lambda - \lambda_0 - \left(\vec{s_k}\cdot\vec{V}_{\varphi,j}\right)\frac{\lambda_0}{c}\right]^2}{2w_j^2} \right\} ds_k, \tag{3}$$

where λ_0 is the central wavelength without the Doppler shift, c is the speed of light, $\vec{V}_{\varphi,j}$ is the toroidal velocity vector, $\vec{s_k}$ is a unit vector along chord k, and w_j is expressed as

$$w_j = \lambda_0 \sqrt{\frac{k_B T_{i,j}}{mc^2}}, \tag{4}$$

where $T_{i,j}$ is the ion temperature, k_B is the Boltzmann constant, and m is the ion mass. s_k is a one-dimensional coordinate system along chord k, and its origin is located at the foot of the perpendicular line from the torus axis to the viewing chord. s_{kj} is a position of the intersection between chord k and the outer boundary of shell j. Note that $s_{k(k+1)} = 0$. γ_k is a factor that compensates for small errors in $\varepsilon(R)$ produced by the Abel inversion. It is obtained so as to satisfy the following relation:

$$I_A(\eta_k) = 2\gamma_k \int_0^{s_{k1}} \varepsilon(s_k) ds_k, \tag{5}$$

where η_k is η for chord k.

The measured spectral shape is distorted because of the instrumental function. Thus, a spectrum measured on chord k ($M_k(\lambda)$) is expressed as the convolution of the instrumental function and chord-integrated spectrum expressed as Eq. (2).

T_i and $\vec{V}_\varphi$ in shell 1, *i.e.* $T_{i,1}$ and $\vec{V}_{\varphi,1}$, respectively, can be determined by fitting $M_1(\lambda)$ to a spectrum measured on chord 1. Then $T_{i,2}$ and $\vec{V}_{\varphi,2}$ in shell 2 can be determined using $T_{i,1}$ and $\vec{V}_{\varphi,1}$ and by the fitting to a spectrum measured on chord 2. Using similar procedures, we can sequentially determine T_i and $\vec{V}_\varphi$ in all the shells from the outboard side. The uncertainties in the obtained parameters were estimated from the standard deviations of the weighted fitting. Random and systematic errors were considered as the weight. Random errors mainly originate from the plasma, detector, and shot noise and were estimated from the standard deviations of signals without any emission lines. Systematic errors include errors that originate from wavelength calibration and approximations of the instrumental function, ε, and the parameters in outer shells except for shell 1.

3.2. Density estimation

The density of C^{2+} ions was derived from emissivity. The emissivity of the transition from state p to state q is expressed as

$$\varepsilon = \frac{h\nu}{4\pi} n_i(p) A(p,q), \tag{6}$$

where h is the Planck constant, ν is the frequency of the transition, $n_i(p)$ is the ion density of the upper state p, and $A(p,q)$ is the spontaneous emission coefficient of the transition [12]. Then, the ion density of the ground state $n_i(1)$ was estimated from $n_i(p)$ on the assumption of the corona equilibrium:

$$C(1,p) n_i(1) n_e = \sum_l A(p,l) n_i(p), \tag{7}$$

where $C(1,p)$ is the rate coefficient for electron-impact excitation from

the ground state to state p [13] which depends on T_e. The summation on the right-hand side shows the sum for all the allowed transitions. As shown in this formula, the values of n_e and T_e are required. We have interpolated the distributions of n_e and T_e to derive the continuous distributions [14]. Errors of the interpolated n_e and T_e were estimated by the same steps as that for emissivity, except that errors of the data were used as the standard deviation instead of performing steps (I) and (II).

4. Results and discussion

We applied the inversion method to the measured spectra in discharges (i)–(iii). Note that 10 viewing chords were removed for discharge (ii) because of a low S/N ratio or the superposition of signals coming from X-rays. The evaluated radial distributions of ε, V_φ, and T_i are shown in Figs. 6(c)–(e), and I_A and V as functions of η are shown in Figs. 6(a) and (b), respectively. For discharges (i) and (iii), the spatial points in Figs. 6(d) and (e) are smaller than those in Figs. 6(a) and (b) because the measured spectra could not be expressed as $M_k(\lambda)$. The three types of discharge have different toroidal velocity profiles. In the core region, V_φ was found to be almost zero in discharge (i), but co-I_p flows of 10 and 4 km/s were observed in discharges (ii) ($R < 0.4$ m) and (iii) ($R =$ 0.6–0.7 m), respectively. In the SOL regions of discharges (ii) and (iii), velocities of up to 20 km/s were observed. These flows were in the same direction as that of the Pfirsch–Schlüter flow [15,16] despite the different directions of the toroidal magnetic field.

For the other parameters ε and T_i, ε peaked near the peak positions of n_e for all the discharges. T_i was the largest in discharge (ii) owing to the largest T_e and the shortest ion temperature relaxation time with electrons, which is caused by the largest n_e [10]. In discharge (ii), T_i peaked near the resonance layer, where T_e also peaked.

Since the error bars in V_φ do not include any errors produced by the discretized approximation in the shell model, we estimated it using model data of ε, V_φ, and T_i. We used three types of model data, (i), (ii), and (iii), shown with the dashed lines in Figs. 7(c)–(e). The data were produced to have similar radial distributions to those measured in discharges (i)–(iii). We calculated chord-integrated spectra for each viewing chord, and to these spectra, Gaussian noises were added with standard deviations of comparable magnitudes to those in the experiments. The calculation was conducted on the axes of the viewing chords.

Then, we applied the inversion method to the synthesized spectra. The results are shown in Figs. 7(c)–(e), and I_A and V are shown in Figs. 7 (a) and (b), respectively. The differences between the assumed model data and the inversion results for ε, V_φ, and T_i are less than 3.5 pW m^{-2} sr^{-1} nm^{-1}, 1.7 km/s, and 2.3 eV for model (i), 3.8 pW m^{-2} sr^{-1} nm^{-1}, 1.4

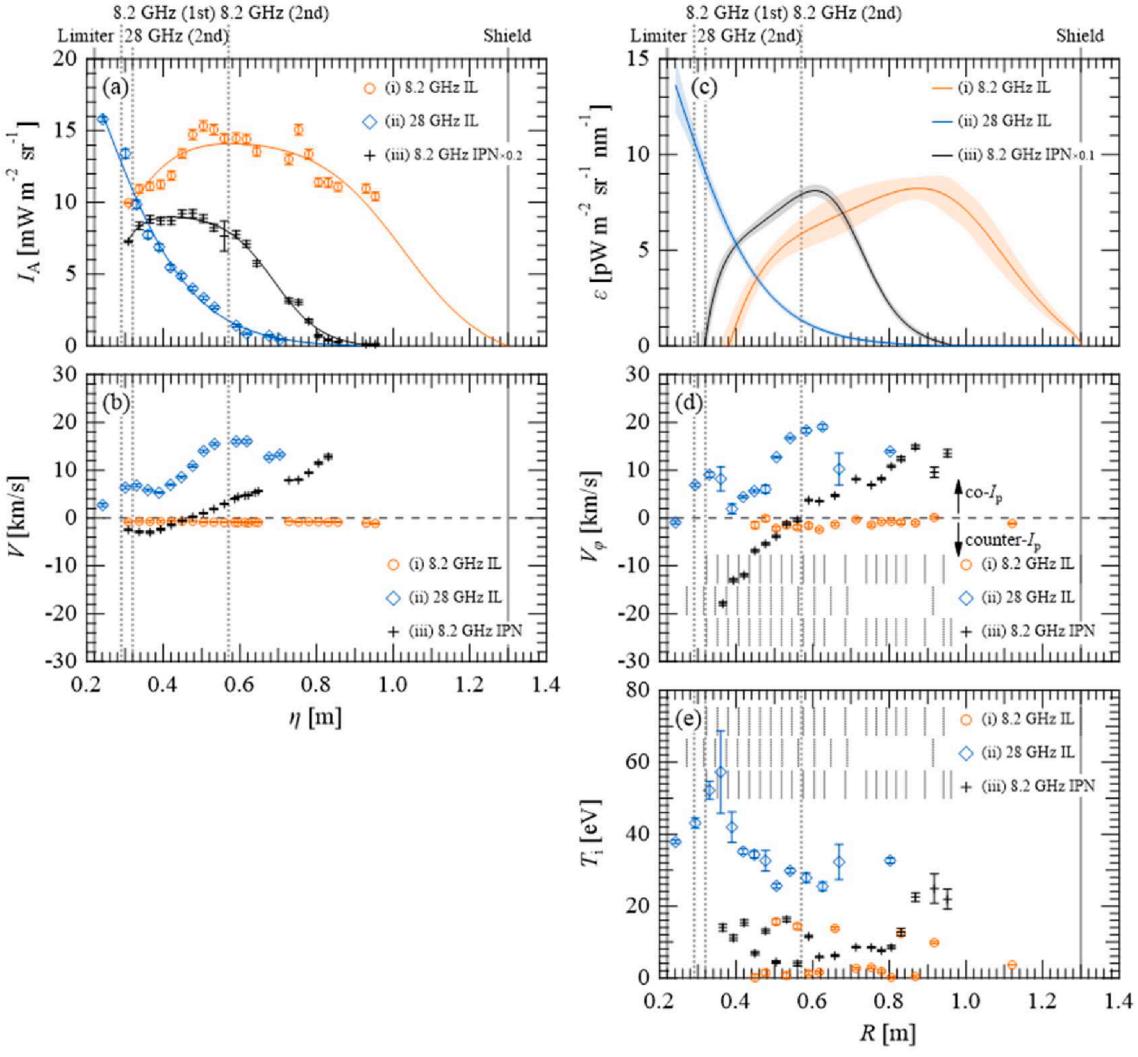

Fig. 6. η-direction distributions of (a) intensity I_A and (b) emissivity-weighted velocity V, and radial distributions of (c) emissivity ε, (d) toroidal velocity V_φ, and (e) ion temperature T_i. Solid lines in (a) are interpolated curves of I_A. Long solid vertical lines show the positions of the inboard limiter (Limiter) and radiation shield (Shield). Dotted vertical lines show the positions of the resonance layers for 8.2 GHz ECH (8.2 GHz (1st) and 8.2 GHz (2nd)) and 28 GHz ECH (28 GHz (2nd)). Short vertical dotted lines shown in (d) and (e) show the boundaries of shells used for the inversion method, which are different for different types of discharge.

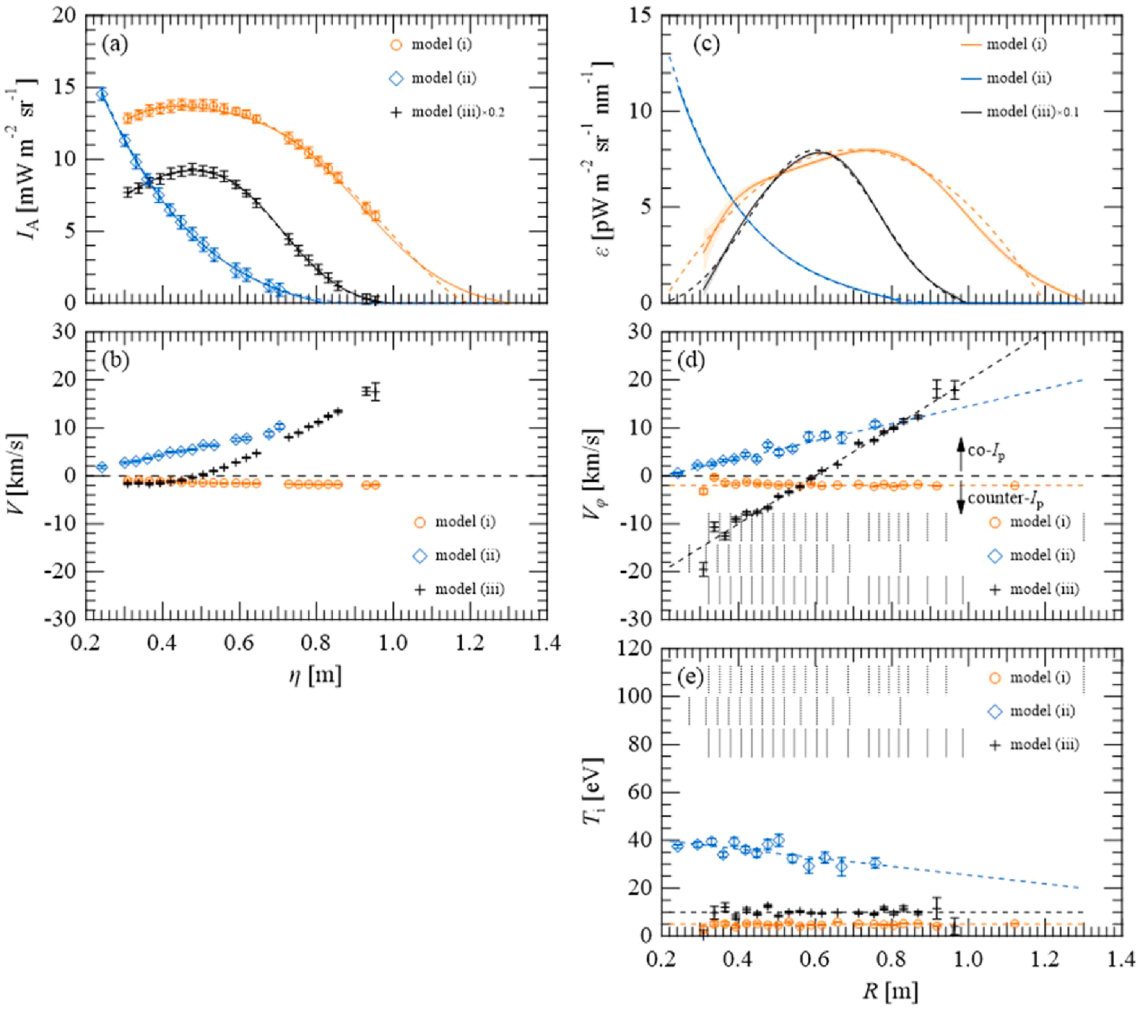

Fig. 7. Validation of inversion method. Dashed lines in (c)–(e) show the values of models used for the validation. Dashed lines in (a) are calculated from the model profile of ε shown in (c). Markers and solid lines in (a) are chord-integrated intensity I_A calculated from the area of the synthesized spectra and interpolated curve of I_A, respectively. Markers in (b), (d), and (e), and solid lines in (c) are values reconstructed by the inversion method.

km/s, and 5.6 eV for model (ii), and 0.58 pW m^{-2} sr^{-1} nm^{-1}, 5.0 km/s, and 10.0 eV for model (iii), respectively. The differences in V_φ are found to be less than 2 km/s except for the inboard side region in model (iii), where the emissivity is small. Also, it was shown that the effect of the chord integral is large for model (iii) but small for models (i) and (ii), as can be seen in Figs. 7(b) and (d).

The radial distribution of n_i is shown in Fig. 8. For discharges (i) and (ii), n_i increased near the outer boundary of emission, R_{end}, because the rate coefficient $C(1,p)$ decreased with the decrease in T_e (see Eqs. (6) and (7)). The estimated n_i was larger than n_e for some regions, where the assumption of the corona equilibrium was inappropriate. All the discharges had peaks near the inboard limiter, which implies that the source of carbon was the limiter.

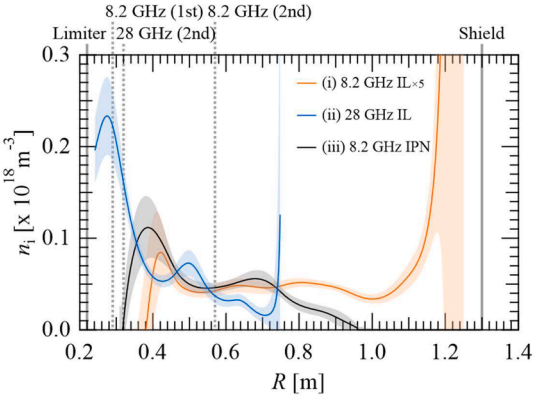

Fig. 8. Radial distributions of ion density. Solid vertical lines show the positions of the inboard limiter (Limiter) and radiation shield (Shield). Dotted vertical lines show the positions of the resonance layers for 8.2 GHz ECH (8.2 GHz (1st) and 8.2 GHz (2nd)) and 28 GHz ECH (28 GHz (2nd)).

5. Conclusions

We developed a spectroscopic system with multiple viewing chords and an inversion method to measure radially resolved C^{2+} ion toroidal velocity in the QUEST midplane. We measured the magnetic field configuration dependence of flow velocity in three types of discharge: (i) 8.2 GHz IL, (ii) 28 GHz IL, and (iii) 8.2 GHz IPN. The evaluated flow velocities were almost zero in the core regions of discharge (i) but 10 and 4 km/s in the co-I_p direction in core regions of discharges (ii) and (iii), respectively. In the SOL regions of discharges (ii) and (iii), the flow velocities were up to 20 km/s, and their directions were the same as that

of the Pfirsch–Schlüter flow [15,16].

CRediT authorship contribution statement

N. Yoneda: Conceptualization, Methodology, Software, Validation, Formal analysis, Investigation, Data curation, Writing - original draft, Visualization. **T. Shikama:** Conceptualization, Validation, Writing - review & editing, Visualization, Supervision, Funding acquisition. **K. Hanada:** Validation, Investigation, Supervision, Project administration, Funding acquisition. **S. Mori:** Methodology, Software, Validation, Investigation, Data curation. **T. Onchi:** Investigation. **K. Kuroda:** Investigation. **M. Hasuo:** Validation, Writing - review & editing, Supervision, Project administration. **A. Ejiri:** Investigation. **K. Matsuzaki:** Formal analysis, Investigation, Data curation. **Y. Osawa:** Formal analysis, Investigation, Data curation. **Y. Peng:** Investigation. **Y. Kawamata:** Investigation. **S. Sakamoto:** Investigation. **H. Idei:** Investigation. **T. Ido:** Investigation. **K. Nakamura:** Investigation. **Y. Nagashima:** Investigation. **R. Ikezoe:** Investigation. **M. Hasegawa:** Investigation. **A. Higashijima:** Investigation. **T. Nagata:** Investigation. **S. Shimabukuro:** Investigation.

Declaration of Competing Interest

The authors declare that they have no known competing financial interests or personal relationships that could have appeared to influence the work reported in this paper.

Acknowledgements

This work was supported by Mori Manufacturing Research and Technology Foundation, bilateral collaboration programs of NIFS (NIFS19KUTR140, NIFS20KUTR156), and collaborative research program of RIAM, Kyushu University (30FP-38). We would like to thank the staff members of the machine shop of Kyoto University for their help with the fabrication of the spectroscopic system.

References

[1] C.B. Forest, Y.S. Hwang, M. Ono, D.S. Darrow, Phys. Rev. Lett. 68 (1992) 3559, https://doi.org/10.1103/PhysRevLett.68.3559.
[2] T. Yoshinaga, M. Uchida, H. Tanaka, T. Maekawa, Phys. Rev. Lett. 96 (2006), 125005, https://doi.org/10.1103/PhysRevLett.96.125005.
[3] K. Mishra, H. Zushi, H. Idei, T. Onchi, M. Hasegawa, K. Hanada, QUEST Team, IEEE Trans. Plasma Sci. 44 (2016) 441, https://doi.org/10.1109/TPS.2016.2522765.
[4] H. Idei, T. Kariya, T. Imai, K. Mishra, T. Onchi, O. Watanabe, H. Zushi, K. Hanada, J. Qian, A. Ejiri, et al., Nucl. Fusion 57 (2017), 126045, https://doi.org/10.1088/1741-4326/aa7c20.
[5] K. Mishra, H. Zushi, H. Idei, M. Hasegawa, T. Onchi, S. Tashima, S. Banerjee, H. Hanada, H. Togashi, T. Yamaguchi, A. Ejiri, et al., Nucl. Fusion 55 (2015), 083009, https://doi.org/10.1088/0029-5515/55/8/083009.
[6] N. Yoneda, T. Shikama, H. Zushi, K. Hanada, A. Fujikawa, T. Onchi, K. Kuroda, K. Nii, M. Hasuo, M. Hasegawa, et al., Plasma Fusion Res. 13 (2018) 3402087, https://doi.org/10.1585/pfr.13.3402087.
[7] T. Yamaguchi, A. Ejiri, J. Hiratsuka, Y. Takase, Y. Nagashima, O. Watanabe, T. Sakamoto, T. Ohsako, B. Il An, H. Kurashina, et al., Plasma Fusion Res. 5 (2010) S2092, https://doi.org/10.1585/pfr.5.S2092.
[8] S. Mori, T. Shikama, K. Hanada, N. Yoneda, A. Kuzmin, M. Hasuo, H. Idei, T. Onchi, A. Ejiri, Y. Osawa, et al., Atoms 8 (2020) 44, https://doi.org/10.3390/atoms8030044.
[9] S.I. Braginskii, Reviews of Plasma Physics, Consultants Bureau, New York 1 (1965) 205.
[10] NRL Plasma Formulary, 2018, pp. 34–35 (https://www.nrl.navy.mil/ppd/sites/www.nrl.navy.mil.ppd/files/pdfs/NRL_FORMULARY_18.pdf).
[11] R.P. Golingo, U. Shumlak, Rev. Sci. Instrum. 74 (2003) 2332, https://doi.org/10.1063/1.1556956.
[12] NIST Atomic Spectra Database (https://www.nist.gov/pml/data/asd.cfm).
[13] Y. Itikawa, S. Hara, T. Kato, S. Nagasaki, M.S. Pindzola, D.H. Crandall, ADNDT 33 (1985) 149, https://doi.org/10.1016/0092-640X(85)90025-7.
[14] C.H. Reinsch, Numer. Math. 10 (1967) 177, https://doi.org/10.1007/BF02162161.
[15] A.V. Chankin, D.P. Coster, N. Asakura, G. Corrigan, S.K. Erents, W. Fundamenski, H.M. Müller, R.A. Pitts, P.C. Stangeby, M. Wischmeier, Nucl. Fusion 47 (2007) 762, https://doi.org/10.1088/0029-5515/47/8/006.
[16] P.C. Stangeby, The Plasma Boundary of Magnetic Fusion Devices, Institute of Physics Publishing, London, 2000, pp. 561–563.